A Rising Star: Truxene as a Promising Hole Transport Material in Perovskite Solar Cells

Kun-Han Lin[†], Antonio Prlj[†] and Clémence Corminboeuf[†]

Laboratory for Computational Molecular Design, Institute of Chemical Sciences and Engineering, Ecole polytechnique fédérale de Lausanne (EPFL), CH-1015 Lausanne, Switzerland.

Abstract: Truxene and its derivatives have been extensively employed for various applications and are considered as promising dopant-free hole transport materials (HTMs) in perovskite solar cells (PSCs). Yet, a systematic exploration of their performance for this specific application remain lacking. Here, multiscale simulations are used to investigate the key structure-property relationships of truxene derivatives featuring distinct variations to the parent core. Specifically, the role of heteroatoms, alkyl chains, and substitution site on the most relevant electronic, transport, and stability properties to high performing PSCs are assessed. Our findings demonstrate that each of the considered truxenes are potential alternatives to the current state-of-the-art HTM Spiro-OMeTAD.

Introduction

Due to their high power conversion efficiency (PCE), solution processability, and relatively low production cost,[1,2] organic-inorganic metal halide perovskite solar cells (PSCs) are tremendously attractive. Efficient light absorbing perovskites such as methylammonium lead iodide ($MAPbI_3$), exhibit wide absorption ranges over the complete visible solar spectrum.[3] While bare perovskite materials display ambipolar transport, high charge carrier mobility, and long charge carrier lifetimes that facilitate the design of hole/electron transport layer (HTL/ETL) free PSCs,[4-6] their corresponding PCE have not exceeded 14%. On the other hand, PSCs containing hole transport layers have reached PCEs over 20%.[7] Clearly, HTLs are highly beneficial, if not necessary for high-performing PSCs[8,9] making it crucial to design and test suitable hole transport materials (HTMs).[10,11]

Since Grätzel and Park's incorporation of Spiro-OMeTAD into the first solid-state PSC in 2012,[12] it has become the prevalent HTM choice. However, its high synthetic cost (~$\$600 g^{-1}$) and complicated purification procedure prevent large-scale commercial production.[13,14] In addition, pristine Spiro-OMeTAD suffers from relatively poor hole mobility ($\mu = 2\times10^{-5}$–$2\times10^{-4} cm^2V^{-1}s^{-1}$).[15-18] In practical PSC device fabrication, Spiro-OMeTAD and other HTMs with low hole mobilities are usually doped with ionic additives such as bis- (trifluoromethylsulfonyl)imide lithium salt (Li-TFSI) to increase their conductivity and enhance the overall PSC performance.[16,19] Yet these additives are detrimental to the long-term stability of PSCs due to their deliquescent nature.[20] Consequently, dopant-free HTMs with high hole mobility arise as an appealing alternative, affording high PCE without simultaneously sacrificing the device stability.[14,20-26]

Among the dopant-free HTMs reported to date, truxene-based HTMs are promising candidates exhibiting a much higher hole mobility and similar glass transition temperature (T_g) compared to Spiro-OMeTAD, leading to PSCs with high PCE and good thermal stability.[25,27,28] Following its first reported synthesis in 1894, truxene and its derivatives have been exploited for diverse applications - non-linear optics, two-photon absorption, transistors, organic light-emitting diodes, molecular resistors, lasers, liquid crystals, supercapacitors, and photovoltaics – thanks to the feasibility and variety of peripheral functionalizations.[25,29,30] However, in contrast to other applications, only a surprising small number of truxene HTMs have been investigated for PSCs applications[25,27,28,31–34] despite the virtually infinite number of structural possibilities. The purpose of this work is thus to address this gap and establish the key features of truxene-based materials that lead to promising HTMs for PSCs.

An ideal HTM for a PSC should fulfill several requirements[35] that can be categorized into three main aspects: electronic properties, hole transport properties and stability (also see Scheme 1), discussed below.

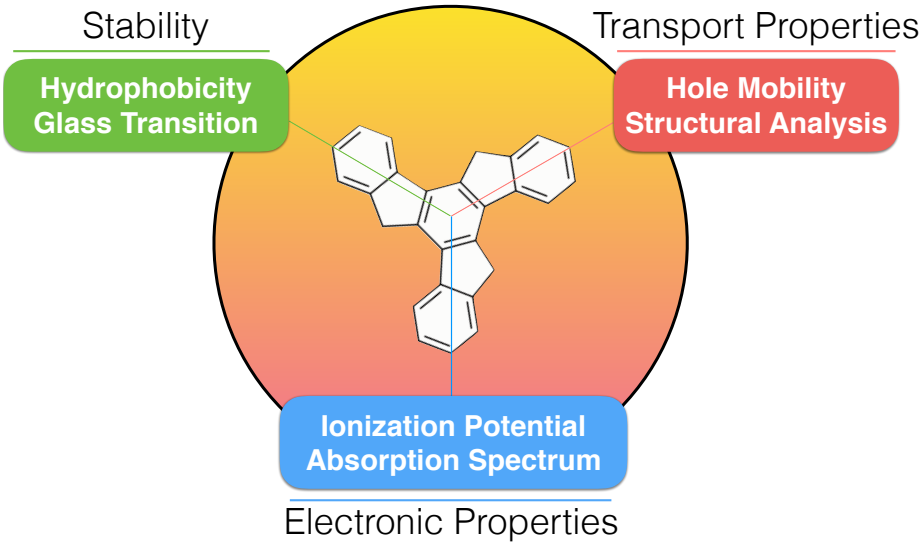

Scheme 1. Critical properties for hole transport materials in perovskite solar cell.

(1) Electronic properties: (a) A suitable energy level alignment between the perovskite and the HTL would facilitate the hole injection and suppress the recombination at the interface, ultimately maximizing the open circuit voltage (V_{oc}).[23,36,37] To fulfill this requirement, the HTM should possess an ionization potential (IP; sometimes approximated as minus HOMO) close to, but not higher than the IP, (sometimes referred to as minus valence band maximum, VBM) of a given perovskite material:[38,39]

$$\Delta IP = IP_{HTM} - IP_{Perovskite} > 0 \quad (1)$$

A too large ΔIP would reduce the efficiency of the hole injection and result in a poor PCE.[22,40] Alternatively, a large negative ΔIP leads to a low V_{oc} that decreases the PCE. (b) An HTM should

exhibit a reduced absorption in the visible spectrum to minimize parasitic absorption and improve the solar power conversion efficiency.[41,42]

(2) Hole transport properties: The injection into the HTL at the perovskite/HTL interface is followed by the free hole carrier transport to the anode.[43] Accordingly, an ideal dopant-free HTM should possess a high intrinsic hole mobility ($>10^{-4}$ $cm^2V^{-1}s^{-1}$) that facilitates hole transport and prevents charge recombination at the interface.[44] High hole mobility may also lead to higher short-circuit current density which enhances the PCE.[45] Note that the mobility of an organic crystal is generally superior to its amorphous phase. However, the latter produces a uniform perovskite/HTM interface that results in a more efficient hole injection, especially in the mesoporous-structured PSCs.[27,35] Hence, previously reported mobilities are mainly based on the amorphous morphology of a given organic molecule.[44] Only the amorphous phase will thus be considered herein.

(3) Stability: (a) Highly hydrophobic HTMs are beneficial as they act as a protective layer boosting overall stability by retarding the ingress of moisture and, in turn, slowing the degradation of the perovskite.[22,46–50] Experimentally, the degree of hydrophobicity can be measured by a water contact angle (WCA).[25,49,51] The higher the WCA, the larger the hydrophobicity and the better the protection of the underlying perovskite layer. (b) Aside from perovskite degradation in the presence of water, the inherent thermal instability of the HTMs comes as another source of possible degradation. Because of their amorphous nature, organic HTMs can undergo a second order phase transition at the glass transition temperature T_g. Since operation temperatures ranging from 60-80 °C are not unusual for practical solar cells, HTMs with relatively low T_g may suffer from significant thermal stress that might eventually deteriorate the performance of the PSC device.[52] Therefore, identifying high-T_g HTMs is also of great importance.

In this work, the truxene core has been selected owing to its inherent high mobility, which eliminates the need for additives and makes truxene molecules efficient dopant-free HTMs in high-performance PSCs.[25,27,33] Analysis of these truxene derivatives revealed structure-property relationships that are highly relevant to PSCs possessing both high performance and high stability. Our computational results agree well with the recent experimental findings by Huang *et al*., who have shown that TruxC-hex-2 (Trux-OMeTAD) is a very promising HTM, with a 18.2% PCE.[25] To the best of our knowledge, this is the first computational work in which nearly every key intrinsic property of HTMs for PSCs have been thoroughly analyzed. Our results provide key insights into the rational design of truxene-based HTMs and, moreover, deliver a broad design strategy with an accompanying comprehensive computational protocol that for rationally developing HTMs and PSCs with superior performance.

Results

Molecular Design

The examined truxene derivatives are displayed in Figure 1 with the nomenclature used thorough. The truxene core carrying three methoxydiphenylamine groups (OMeDPA) on substitution sites 3, 8, 13, is named TruxC. The effect of the heteroatom substitution is investigated by considering heterotruxenes such as triazatruxene (nitrogen, TruxN) and thiatruxene (sulfur, TruxS), which have been synthesized and considered as potential candidates in organic electronics.[53,54] We anticipate that altering the heteroatom in the truxene core will tune the ionization potential (IP) and ultimately lead to a desirable V_{oc}. In fact, it has been demonstrated that superior

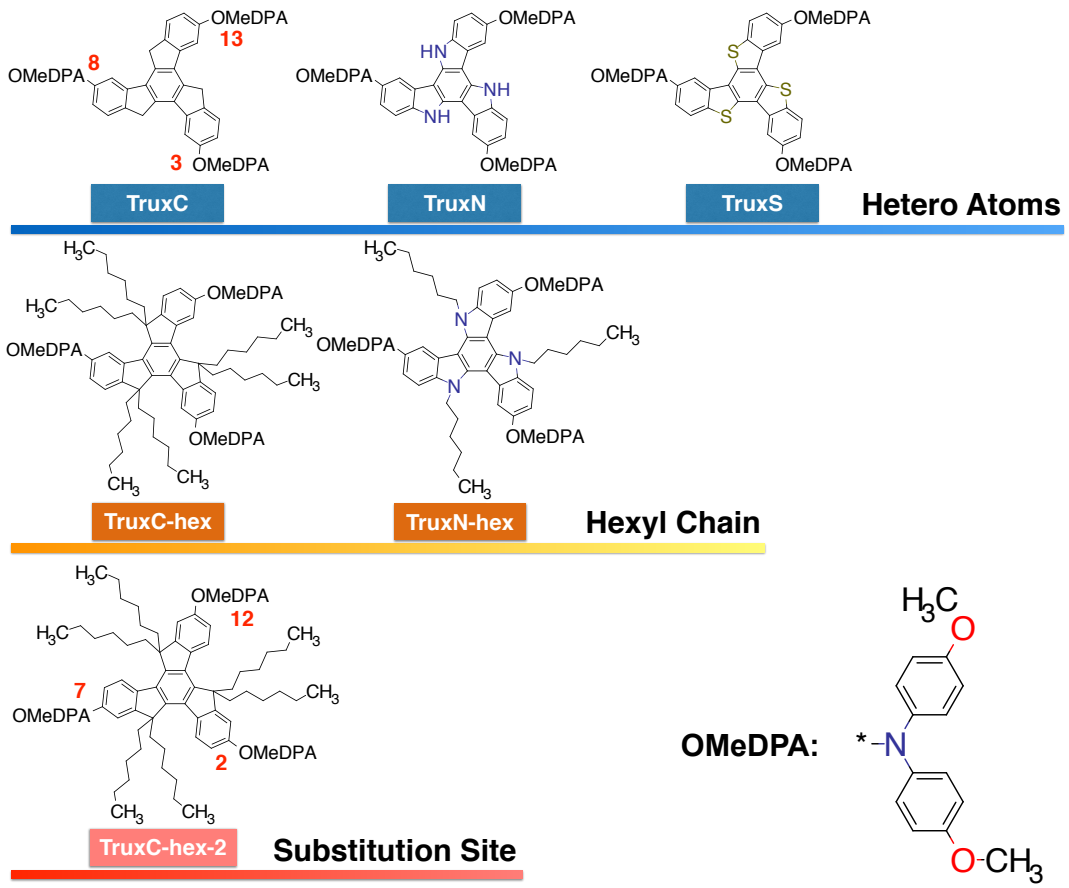

Figure 1. Truxene derivatives considered in this work.

hole transport properties can be achieved via substitution of two heteroatoms.[55,56] Even though truxene derivatives without alkyl chains are already solution processable,[57] alkyl chains have found wide use as solubilizing moieties in organic solvents. However, addition of alkyls chains can modify the molecular packing and has sizable effect on charge transport.[58,59] For this reason, their influence on each of the properties is also of interest. A methylene unit was thus replaced with a C-2(hexyl) and an N-hexyl to form the TruxC-hex and TruxN-hex structures. Finally, inspired by the work by Zhang *et al*.[60] regarding the 3D molecular structural effect on the overall PSC performance, we altered the substitution sites of OMeDPA from 3, 8, 13 to 2, 7, 12, thereby creating TruxC-hex-2. The computational estimates of the transport properties of these derivatives require extensive multiscale simulations, which are detailed in the computational detail section.

Electronic Properties

Ionization potentials were computed using ΔSCF method with different density functionals and methods suggested by Li *et al*.[61,62] of which ΔSCF method with B3LYP functional and methods suggested by Li *et al*. had an excellent agreement with experiment (see ESI). For simplicity, discussions on IP refer to results by ΔSCF method with B3LYP functional. The energy level alignments shown in Figure 2 illustrate the effect of the IP tuning through heteroatom substitution. Swapping C for N decreases the IP by 0.13 eV, while sulfur increases in to 5.35 eV, close to $MAPbI_3$(5.43 eV). The hexyl chains enlarge the IPs by ~0.1 eV for both TruxN and TruxC, aligning the HOMO of TruxC-hex nearly perfectly with the valence band maximum of $MAPbI_3$. A closer inspection of the geometries of TruxC-hex and TruxN-hex reveals that the relative proximity between the hexyl chains and the neighboring OMeDPA groups influence the dihedral angles between the phenyl groups of OMeDPA and the planar truxene core. This geometrical constrain directly correlates with the increase in IP (see ESI). Yet, the benefit associated with the

incorporation of alkyl-chains is lost if the substitution sites of OMeDPA are varied (TruxC-hex → TruxC-hex-2, IP=5.14 eV). Overall, these truxene variants outperform Spiro-OMeTAD in terms of ΔIP. Among them, TruxS and TruxC-hex exhibit the most promising energy alignment with the perovskite layer suggestive of a high V_{oc}.

UV-Visible absorption spectra were computed using linear response time-dependent density

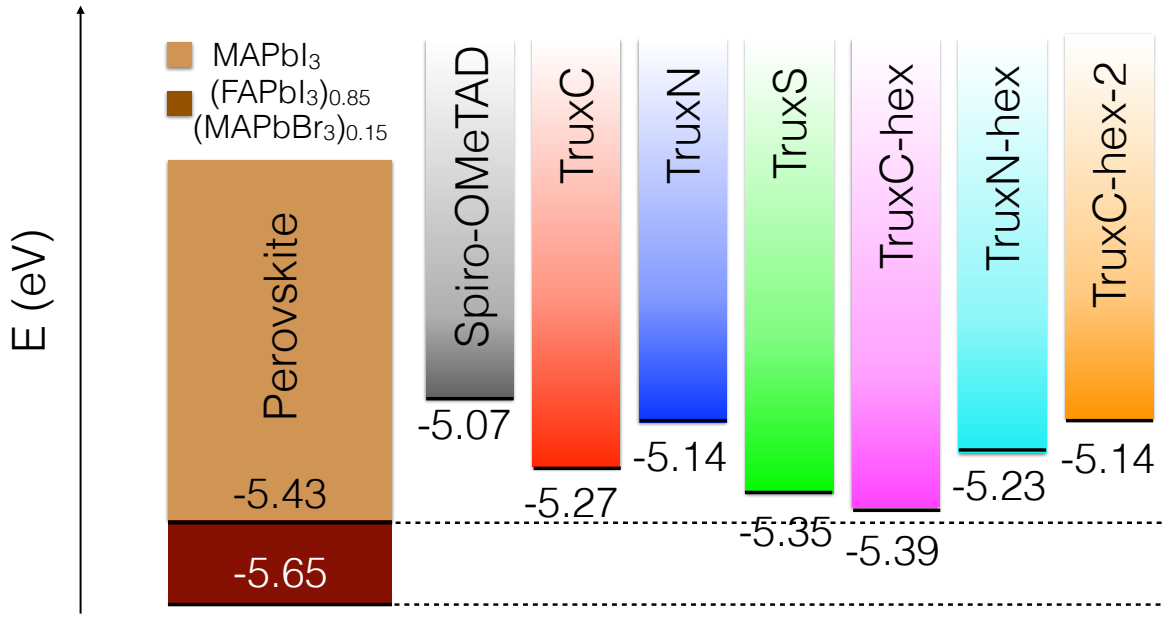

Figure 2. Energy level diagram for perovskite, Spiro-OMeTAD and truxenes. The numerical values of Spiro-OMeTAD and truxenes are minus computed IPs the B3LYP/6-31G(d,p) level. The VBM of perovskites are taken from ref 26 and 33.

functional theory (see computational details) for Spiro-OMeTAD and truxenes (Figure 3). The extent of overlap between the two spectra (absorption and solar irradiance) is indicative of parasitic loss. Small spectral overlap is preferred since only little amount of solar energy would be wasted (see Figure S5). The computed spectra are in reasonable agreement with experimental results (Table S4). In the visible range, Spiro-OMeTAD shows a larger overlap with the solar spectral irradiance as compared to truxenes. Moreover, the ionic additives create a number of oxidized

Spiro-OMeTAD molecules, which enlarge the absorption in the visible range and result in a larger parasitic loss (Figure S5).[42,64] In the truxene series, the heteroatom substitution increases the spectral overlap, especially for the nitrogen case (larger peaks at 368 nm). Altering the OMeDPA sites induces a higher absorption peak at 385 nm, which makes TruxC-hex-2 the largest overlap with the solar spectrum among all of our truxene derivatives. Overall, truxenes considered here show smaller overlap with solar spectrum as compared to Spiro-OMeTAD. Furthermore, dopant-free truxenes can avoid introducing additional cation species, leading to lower parasitic loss in visible range. This makes them promising HTM candidates in inverted or tandem PSC design in terms of lower parasitic loss.

Transport Properties

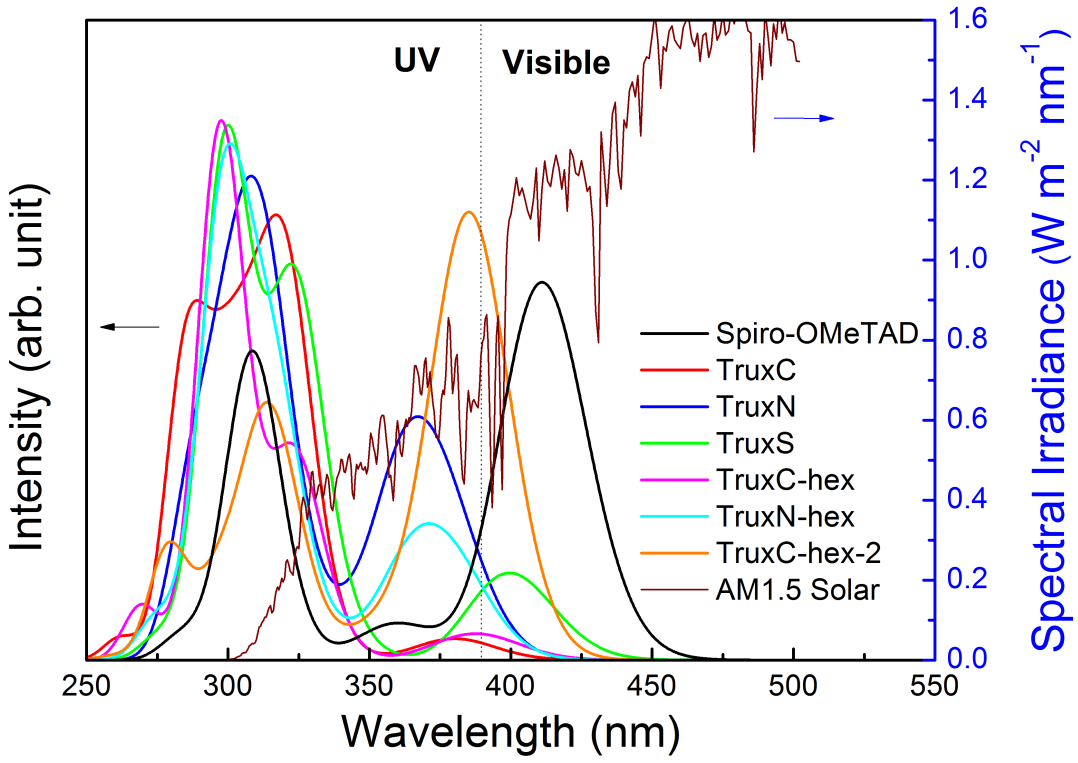

Figure 3. Computed UV-visible absorption spectrum of each molecule at the TD-B3LYP/6-31G(d,p) level and the standard AM1.5 solar spectral irradiance (ASTM G-173; Global Tilt).[63]

Hole transport properties were computed for the amorphous phase of truxenes using a multiscale approach that combines classical molecular dynamics simulations, kinetic Monte Carlo techniques and electronic structure computations (see Computational Details). Non-adiabatic semi-classical Marcus charge-transfer theory[65,66] was applied to evaluate hole transport mobility, in which the high-temperature limit the hopping rate between different sites is defined as:

$$\omega_{ij} = \frac{J_{ij}^2}{\hbar}\sqrt{\frac{\pi}{\lambda k_B T}}\exp\left[-\frac{\left(\Delta E_{ij}-\lambda\right)^2}{4\lambda k_B T}\right] \quad (2)$$

where T is the temperature, J_{ij} is the transfer integral between sites *i* and *j*, ΔE_{ij} is the site energy difference (*i.e.*, $E_i - E_j$) and λ the reorganization energy. Equation (2) shows that, taken together, a smaller reorganization energy (λ) and a larger transfer integral (J) result in faster hole transport. Likewise, smaller energy disorder (σ; spread of the hopping site energy differences) also leads to higher hole mobility.[67,68] Hole mobility along with all these related components of the truxene derivatives are presented in Figure 4. Energy disorder did not show sizable variation upon structural modification. However, a large increase in reorganization energy occurs upon inclusion of hexyl chains (Figure 4a). Varying the substitution sites of OMeDPA can attenuate the unfavorable enhancement in reorganization energy.

The distribution function of the squared transfer integral (Figure 4b) gives a good description of the high value region (10^{-3}~10^{-2} eV^2) that significantly contributes to hole mobility. The effect of the heteroatom is pronounced as illustrated by the largest spread of TruxN, followed by TruxS and TruxC. The hexyl chains deteriorate the electronic coupling between the cores lowering the distribution curve significantly. This deterioration becomes clear when analyzing the radial distribution function (RDF) between the centers of geometry (COG) of the truxene cores as depicted in Figure 4c. The first peaks for the bare truxene are located in the 4-5 Å range. In sharp

contrast, the substituted truxenes show no peak in this region with a sizable band appearing only at larger distances (≥10 Å), which is associated with significantly lower transfer integrals.

The relative arrangement of truxene molecules is best represented by the 2D color maps shown in Figures 5, S10 and S11. Two descriptors, the distance between the COG of the truxene cores (d_{ab}) and the angle between the normal truxene planes (θ_{ab}) are used for the x- and y-axis in

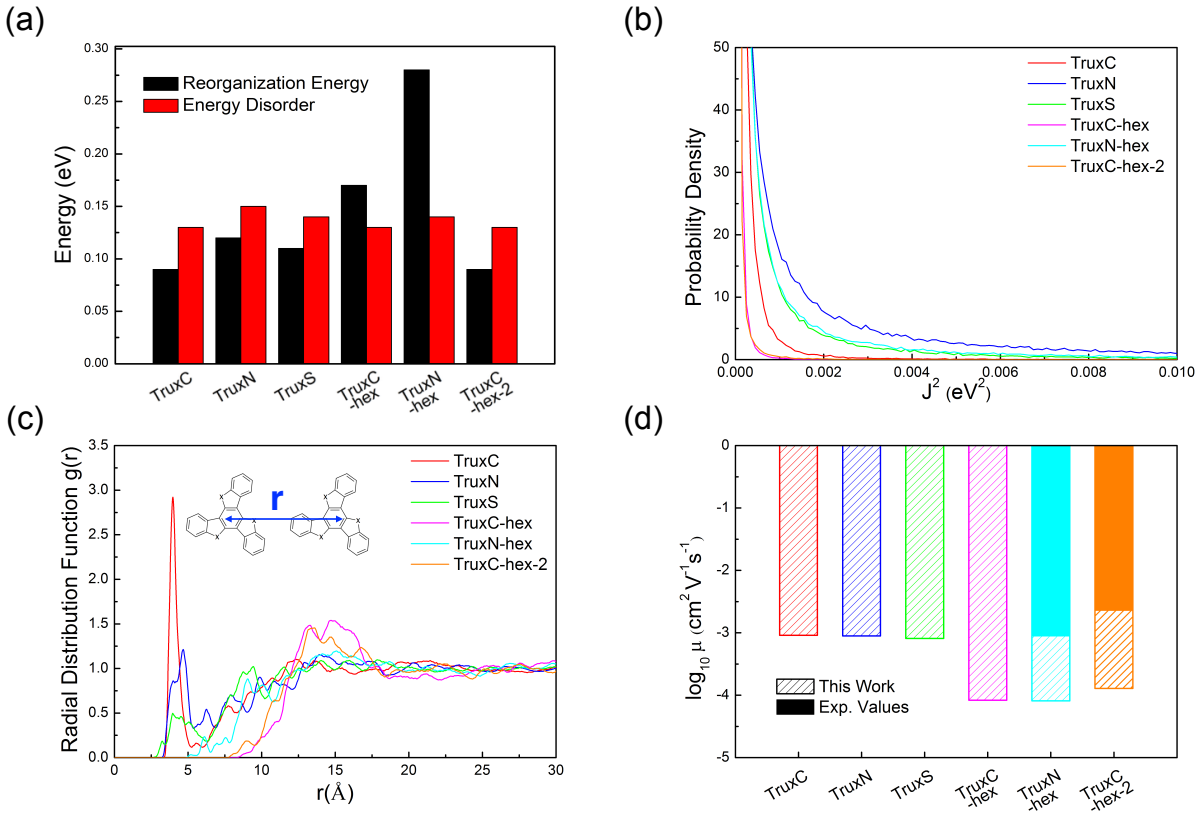

Figure 4. (a) Energy disorder vs. reorganization energy plot, (b) probability density distribution of transfer integral square, (c) radial distribution function between centers of geometry of truxene cores and (d) averaged hole mobility of amorphous phase of each molecule.

Figure 5(a). Each color-coded dot depicts the occurrence of a given configuration along the molecular dynamic trajectory (see computational details) with the color denoting the value of the square of the transfer integral (Figure 5c and 5d). Comparisons of the 2D color maps reveals the presence of a region associated with face-to-face dimer configurations of TruxC, which are absent

in TruxC-hex. These face-to-face configurations possess large J_{ij}^2 *values* (order of 10^{-2}), which promote hole mobility. After examining each case in Figure S10 and S11, it becomes clear that the presence of hexyl chains prevents the favorable face-to-face truxene arrangement. Further analysis of Figure 4(b) and Figure S10, clarifies the wide-spread transfer integrals of TruxN, which arises not only from the higher overall populations around 5 Å, but also from the higher transfer integral ($\sim 10^{-1}$ eV^2) at the same (distance, angle) configurational space compared to TruxC and TruxS. A similar reasoning applied to the comparison of TruxN-hex and TruxC-hex.

The hole mobilities for each molecule are then computed on the basis of all the properties discussed above (Figure 4d). The computed mobilities are systematically one order of magnitude lower than the experimental results, which is consistent with the known underestimation of the transfer integral by the ZINDO method (see computational details).[69]

In the absence of hexyl chains, truxene and heterotruxenes show remarkably similar hole mobilities in the order of 10^{-3} cm^{2}V^{-1}s^{-1}. In contrast, the substituted truxene derivatives exhibit mobilities one order of magnitude lower than the bare analogues in line with the absence of face-to-face arrangements (*vide supra*). Considering the underestimation of the computed hole mobilities, values in the $10^{-3} \sim 10^{-2}$ cm^{2}V^{-1}s^{-1} range are likely to be measured experimentally for the core lacking alkyl chains. Assuming that other conditions remain unchanged, they would outperform the PCE of their counterpart bearing alkyl chains. Also noteworthy is the increase in

hole mobility brought about by modifying the OMeDPA position, which originates from a reduction of the reorganization energy giving a nearly 1.5-fold enhancement (Table S5).

Stability

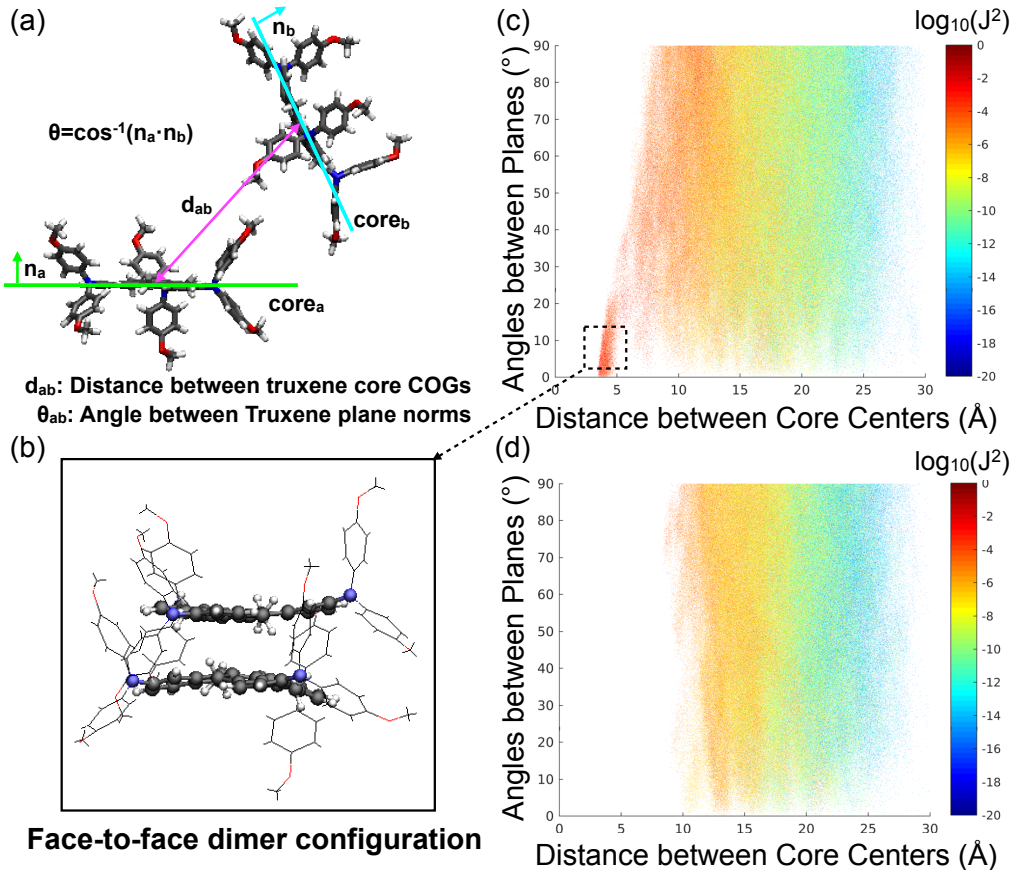

Figure 5. (a) Two descriptors used in 2D color map. (b) Face-to-face dimer configuration of truxene molecules. The 2D map colored with transfer integral square for (c) TruxC and (d) TruxC-hex.

Hydrophobicity was evaluated by computing the water contact angles of Spiro-OMeTAD and the truxene series, as illustrated in Figure 6. Both intrinsic (dopant free) Spiro-OMeTAD and TruxC-hex-2 show good agreement with experimental observations (70°~74.5°[15,48] and 90.4°[25], respectively), which justifies the method utilized here (see Computational Details and ESI). The

WCA ordering for the truxenes without hexyl chains is: TruxC > TruxS > TruxN. The extent of hydrophobicity can be adjusted by incorporating heteroatoms, which leads to differences as large as 13.1° (TruxC vs. TruxN). The inclusion of hexyl chains increases the WCA considerably: by 24.5° for TruxC and 22.8° for TruxN, as expected from the hydrophobic nature of the alkyl chains. Modification of OMeDPA substitution site was found to decrease WCA by ~10°.

Estimations of the *glass transition temperature* are shown in Figure 7. In comparison with

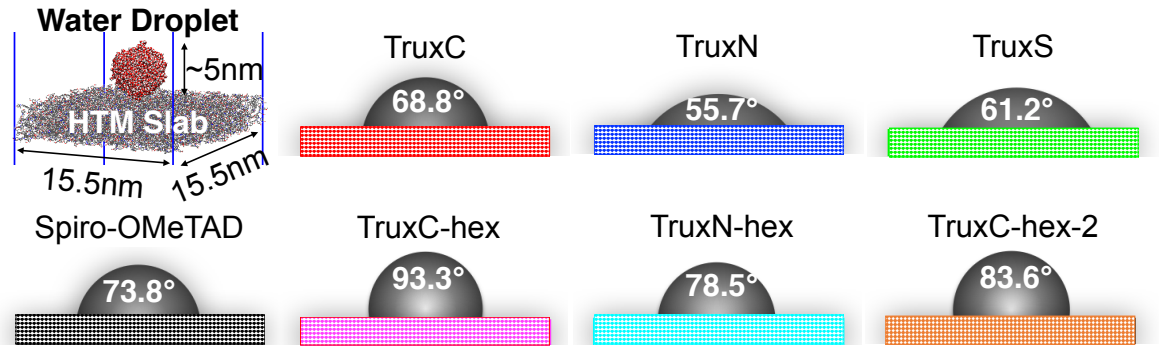

Figure 6. Molecular dynamics simulation cell and computed water contact angle for intrinsic Spiro-OMeTAD and truxenes.

the known experimental values, our T_gs are systematically ~40°C higher for Spiro-OMeTAD and TruxC-hex-2, due to the much faster cooling rate adopted in molecular dynamic simulations.[70] Despite this overestimation, the qualitative comparisons among the truxene derivative is valuable. The heteroatom substitution from C to N and C to S leads to a serious decrease in T_g of 28°C and 36°C, respectively. Adding hexyl chains also reduced T_g by 28°C for TruxC and 10°C for TruxN. A decrease in T_g upon inclusion of long alkyl chains has been previously observed.[71] For small organic molecules, this phenomenon can be explained by the concept of free volume (V_{free}), which has been invoked to elucidate the influence of the chain length (n) on T_g for poly-(n-alkyl methacrylates) polymers.[72] The longer the alkyl chains, the further the molecular separation. This

free volume facilitates the molecular motions, which in turn, lower T_g. V_{free} was evaluated by subtracting the average volume of a molecule in the amorphous phase (V_a) by the volume of molecule in the gas phase (V_g):

$$V_{free} = V_a - V_g \quad (3)$$

Our result confirms that the addition of hexyl chains increases V_{free} by 182 Å^3/molecule for TruxC and 214 Å^3/molecule for TruxN. Changing the substitution sites of OMeDPA as in TruxC-hex-2 also lower T_g in comparison to TruxC.

It should be noted that the computed WCA and T_g of Spiro-OMeTAD are the intrinsic one. We want to stress that since, in practical applications, Spiro-OMeTAD is always doped to

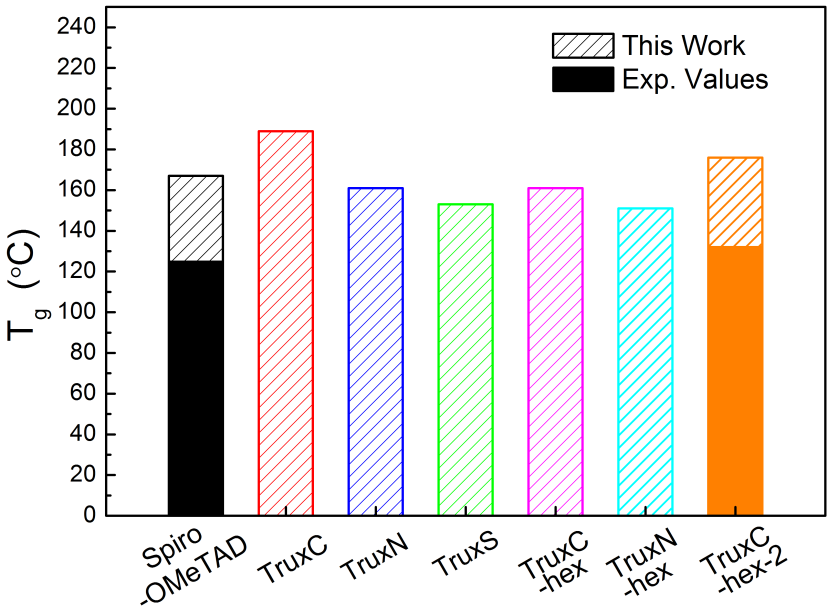

Figure 7. Computed and experimental glass transition temperature. The experimental value of intrinsic Spiro-OMeTAD are taken from ref [52]. The experimental T_g of TruxC-hex-2 is approximated by that of TruxC-propane-2 in ref [28] since it is not available.

compensate for its poor hole mobility, a comparison between dopant free truxenes and doped

Spiro-OMeTAD is more reasonable. In this respect, all truxenes considered here outperform the doped Spiro-OMeTAD in terms of both water contact angle (56°)[46] and glass transition temperature (<100°C).[52]

Solubility

Solution-processable HTMs should be soluble in common organic solvents. For this reason, the Hildebrand[73] and Hansen[74] solubility parameters were computed for chlorobenzene to evaluate their relative tendency of the truxenes to dissolve.[75,76] The cores free of hexyl chains tend to dissolve more easily in chlorobenzene than the substituted species (Table S7), likely because the hexyl chains hinder the solvent access and prevent the formation of favorable solute/solvent π -π interactions. At the first glance, this result might appear counter-intuitive since the addition of alkyl chains generally enhances compound solubility in organic solvents. Yet, the factors governing the solubility of a solute in a given solvent are rather complexes and various (e.g., molecular structures, polarity and types of interaction between solute and solvent). If one considers hexane (i.e., alkyl chains) rather than benzene-like solvent, the trends are opposite to that of chlorobenzene following the "like dissolve like" rule. Overall, since TruxC-hex-2 and TruxN-hex have already been shown to be solution processable in common benzene-like organic solvent (chlorobenzene and toluene),[25,27] it is envisioned that other truxenes without hexyl chains will also be processable in these solvents.

Summary

The electronic, structural features, hole transport properties and stabilities of the investigated truxenes and the reference Spiro-OMeTAD (intrinsic and doped) are summarized in Figure 8. The following structure-property relationships emerge from the examination of the different derivatives.

Comparison of TruxC, TruxN and TruxS illustrates the effect of the heteroatom on the IP (increase for TruxS, decrease for TruxN) and parasitic loss (slight increase). The hole mobility remains virtually unchanged but the hydrophobicity and glass transition temperature decrease for TruxS and TruxN. The lower hydrophobicity of the heteroatomic truxenes arises from the enhanced local polarizability induced by the heteroatoms, making the HTM more hydrophilic. This is in line with the various degree of hydrophilic behavior among their small molecule analogues. The solubility in water is pyrrole > thiophene > cyclopentadiene, which corresponds to the order of the WCAs.[77]

The alkyl chains influence every property investigated herein. They act as solubilizing groups (increasing the hydrophobicity) and, somewhat unexpectedly, they decrease the IP of both TruxC and TruxN because of geometrical distortions. The inclusion of hexyl chains also decreases the hole mobility by nearly one order of magnitude (compare TruxC, TruxN with their chain-containing counterparts). The side chains prevent the truxene cores from adopting a face-to-face dimer configurations, associated with a high transfer integral. Finally, the larger hydrophobicity of the substituted truxene is accompanied by an unfavorable decrease in T_g. Based on these observations, we can conclude that adding alkyl chains may be beneficial for the properties of truxene as an HTM, but further studies should to identify the optimal chain length are necessary.

Varying the position of OMeDPA (TruxC-hex vs. TruxC-hex-2) decreases the IP and red-shifts the absorption spectrum. It does reduce the reorganization energy by half while retaining a similar energy disorder and transfer integrals. All this leads to a 1.5-fold larger hole

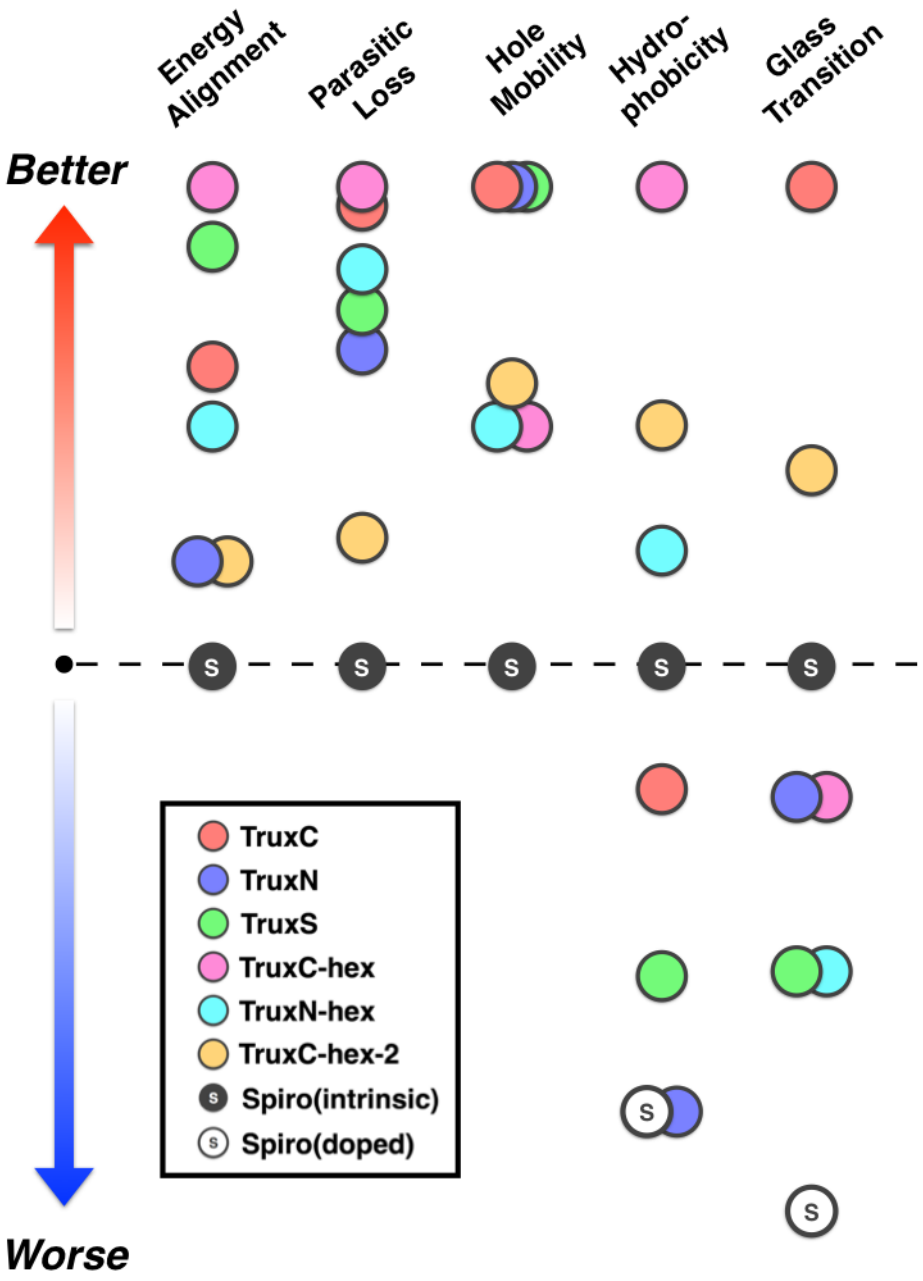

Figure 8. Relative trends in the normalized computed electronic properties, transport properties and stability. The mobility of intrinsic Spiro-OMeTAD[18] and all the properties of doped Spiro-OMeTAD[46,52] are taken from experiment. The maximum point is set with the best truxene in each property and zero point with intrinsic Spiro-OMeTAD. Other points are scaled based on these two references (see ESI).

mobility. Furthermore, the change in substitution site does not deteriorate T_g significantly, but still preserves a high hydrophobicity. These comparisons demonstrate the influence of a substituent and emphasize the impact of the 3D molecular shape on the properties and morphology of the amorphous phase.

Overall, if only the power conversion efficiency of PSCs is considered, TruxS would be the best candidate tested herein owing to its excellent energy alignment and high hole mobility. However, PCE is not the only criterion necessary to create an ideal perovskite solar cell. In terms of stability, TruxC and TruxC-hex-2 would be promising hole transport materials. In addition to their suitable energy level alignment and hole mobility similar to TruxS, TruxC displays a mild hydrophobicity and high thermal stability. TruxC-hex-2, on the other hand, shows a larger ΔIP, medium hole mobility and possesses both high hydrophobicity and thermal stability. As compared to the intrinsic Spiro-OMeTAD, each of these two molecules exhibit a better performance in every facet. Thus, these molecules represent promising alternatives. Acknowledging that Spiro-OMeTAD must be doped in practical applications, all of the proposed truxene derivatives represent superior alternatives. Simulation protocols such as those discussed in this contribution, rationalize the outstanding performance of TruxC-hex-2 (Trux-OMeTAD)[25] through investigation from a molecular viewpoint by providing concrete structure-property relationship that can serve to identify additional candidates (TruxC and TruxS) for use in perovskite solar cell applications.

Conclusions

We have employed sophisticated multiscale modeling techniques to derive structure-property relationships for several truxene derivatives. The resulting trends in the electronic, transport properties and stability criteria, crucial for achieving the high-performance perovskite solar cell, illustrate the effects of the heteroatom substitution, alkyl chain addition and site alteration.

As a result of this work, several promising HTM candidates were identified as alternatives to Spiro-OMeTAD. A perovskite solar cell with a TruxS HTM, for example, would exhibit high PCE due to good energy alignment and high hole mobility. Furthermore, to ensure long-term performance a compromise between performance and stability is required. In this case, both TruxC and TruxC-hex-2 show great promise, as recently demonstrated by experiment (TruxC-hex-2).[25] Finally, the computational methodology and protocol employed here are broadly applicable for rationally developing HTMs and PSCs with superior performances. Within this context, in the future we intend to complement this rational design strategy with high-throughput screening of the electronic properties of various commonly used cores.

Computational Details

Electronic Properties:

Molecular Geometry

All the geometries of the neutral and cationic molecules were optimized using B3LYP-[78,79]D3BJ[80] in conjunction with the 6-31G(d) all-electron basis set. Computations related to the following section were performed with Gaussian09.[81]

Ionization Potential

The ionization potential (IP) were computed using a ΔSCF (delta self-consistent field) procedure in conjunction with different density functionals and the 6-31G(d,p) basis set (Table S1):

$$IP = \Delta SCF = E_{\mathrm{cN}} - E_{\mathrm{nN}} \quad (4)$$

where E_{nN}/E_{cN} is the total energy of the neutral/charged molecule in neutral geometry.

UV-visible Absorption Spectrum

The UV-vis absorption spectra were computed at the TD-B3LYP/6-31G(d,p) level with the conductor-like polarized continuum (C-PCM)[82] solvent model using tetrahydrofuran. Gaussian broadening with a 0.13 eV σ was adopted to generate the absorption spectrum.

Hole Mobility:

Amorphous Structure Construction

The amorphous assemblies were constructed from a unit cell containing 64 molecules using Packmol.[83] The molecules were first minimized using conjugate gradient algorithm and then equilibrated in the NPT ensemble (500K, 1bar) by performing classical molecular dynamics (MD) simulation. This equilibrated system was then extended to a 2x2x2 supercell with 512 molecules. Further equilibration (500K, 1bar) was performed for 5ns. Finally, a 10ns equilibration in the NPT ensemble (300K, 1bar) followed by another 10 ns for production run serve to generate 1000 snapshots. The simulations were performed under periodic boundary condition using GROMACS package[84,85,86] and the CGenFF[87,88] force field along with charges obtained by the restrained electrostatic potential (RESP)[89] procedure based on HF/6-31G(d,p). The temperature and pressure control used velocity rescaling with a stochastic term[90] (T = 300K, τ_T = 1.0 ps) and an isotropic coupling for the pressure from a Berendsen barostat (P_0 = 1 bar, $\chi = 4.5 \times 10^{-5}$ bar^{-1}, τ_P = 1.0 ps). The time step used in all simulation was 1 fs. Bonds involving H atoms were constrained using Linear Constraint Solver (LINCS) algorithm. A cutoff of 12 Å was applied to the van der Waals interaction through the force-switch mode. As for electrostatic interactions, the particle mesh Ewald (PME) method was employed with a 0.12 nm Fourier spacing.

Hole Mobility Computation

The hole mobilities of the HTMs were computed according to the semi-classical Marcus charge-transfer theory on 200 frames extracted from previous MD trajectories using the VOTCA

package.[69,91] Within this formalism, the charges are assumed to be localized on a single molecule and each molecule is considered as a hopping site. The charge transfer process thus takes place through the hopping between different sites. The high-temperature, which limit the hopping rate between different sites is defined as Equation (3). The reorganization energy was computed by a 4-point method at the B3LYP-D3BJ/6-31G*level:

$$\lambda = E_{\mathrm{nC}} - E_{\mathrm{nN}} + E_{\mathrm{cN}} - E_{\mathrm{cC}} \quad (5)$$

where E_{nN} (E_{cC}) is the total energy of the neutral (charged) molecule in neutral (charged) geometry and E_{nC} (E_{cN}) is the energy of the neutral (charged) molecule in charged (neutral) geometry. The Thole model was used to compute site energy (E_i or E_j), which includes contributions from electrostatic interactions, polarization and external electric field.[69] The partial charges needed in this model for neutral and charged state were generated via CHelpG method[92]. The transfer integral J_{ij} was evaluated considering the HOMO and HOMO-1 simultaneously[93] for every molecular pair ij in the neighbor list. This neighbor list was established for every molecular pair having a distance between their nearest fragments within 7 Å. Once all the parameters necessary to calculate the hopping rate are computed, a 1 ms kinetic Monte Carlo (KMC) simulation was performed using a 10^5 Vcm^{-1} electric field to obtain the hole mobility. For a given snapshot (structure), the KMC simulations were conducted with the electric field in three different directions resulting in a total simulation time that correspond to three times the number of snapshots. Figure S6 illustrates that 200 snapshots (600 KMC simulations) are already sufficient to obtain a statistically meaningful distribution of hole mobility.

Structural Analysis

The construction of the 2Ds map was based on the molecular pairs found in the neighbor list established in for the hole mobility computations. Molecular pairs with a distance between COGs of truxene cores larger than 3 nm was not observed.

Hydrophobicity and Glass Transition Temperature:

Water Contact Angle

We employed soft-confined method to create an amorphous organic solid surface preventing uncontrollable roughness on the surface.[94] The whole simulation procedure is illustrated in Scheme S1. Starting from a supercell with x=y=155.0580 Å and z=310.1160 Å, two xenon crystal walls were placed 120 Å apart. Using Packmol, 512 molecules were then placed between these two walls leading to a sandwich structure. The NVT simulation was then performed at 500K, while gradually decreasing the distance between the two walls until reaching the targeted density for the middle amorphous slabs. For each given specie, the targeted density was chosen as the bulk density. Once the desired density was reached, the system was equilibrated in the NVT ensemble at 300K for 10 ns with fixed walls. Finally, the xenon walls were removed, leaving the amorphous slab ready for further simulations.

The water droplet to put atop the amorphous slab was created from a water cube with 1500 water molecules and equilibrated in the NPT ensemble (300K, 1bar) using the simple point charge model (SPC).[95] This equilibrated cube was then placed into a 110 Å side cubic supercell and equilibrated in the NVT ensemble at 300K to obtain a water droplet. This droplet was placed on the amorphous slab and equilibrated in the NVT ensemble at 300K with fixed slab for 10 ns. The simulation details are similar to *Amorphous Structure Construction* section. The Particle Mesh Ewald approach with the slab correction 3dc was adopted to compute the long-range Coulombic

interactions.[96] The readers can refer to the supporting information to read more about the method employed to extract the WCA from the MD trajectory.

Glass Transition Temperature

Starting from the previous structures with 512 molecules equilibrated under (500K, 1bar), the system was cooled down from 500K to 300K stepwise at 10K intervals under a constant pressure (1bar). For each temperature step, the step size was 2ns, and the final 500 ps was used to collect statistics at a frequency of 0.20 ps. The cooling rate between the successive temperatures was 0.33 K/ps. The simulation details are similar to *Amorphous Structure Construction* section. The T_g is obtained from the intersection of two fitted lines in specific volume-temperature plot. For details, please refer to the supporting information.

The volume of a molecule in the gas phase V_g is the volume enclosed by the electron density isosurface with an isovalue of 0.001 electrons/Bohr^3 computed using B3LYP/6-31G(d,p).

Solubility Parameters:

The Hildebrand solubility parameter (δ_T) is defined as the square root of cohesive energy density (CED). However, this single parameter can only give reasonable prediction for non-polar or slightly polar molecules. In order to broaden its applicability, Hansen further divided the cohesive energy into three intermolecular contributions: dispersive interactions (δ_D), dipole-dipole interactions (δ_P), and hydrogen-bonding interactions (δ_H) as shown in Equation (6):

$$\delta_T = \sqrt{CED} = \sqrt{\delta_D^2 + \delta_P^2 + \delta_H^2} \quad (6)$$

The Hildebrand and Hansen solubility parameter were extracted from the MD simulations. Given that contribution from the hydrogen bond energy is not straightforward,[76] we only reported the contribution from overall Coulombic interaction δ_Q, with the relation:

$$\delta_Q = \sqrt{\delta_P^2 + \delta_H^2} \quad (7)$$

The distance between the truxenes (solute) and chlorobenzene (solvent) in Hansen parameter space is an index for solubility, which is approximated by:

$$R^2 = 4(\delta_{D1} - \delta_{D2})^2 + (\delta_{P1} - \delta_{P2})^2 + (\delta_{H1} - \delta_{H2})^2$$

$$\approx 4(\delta_{D1} - \delta_{D2})^2 + (\delta_{Q1} - \delta_{Q2})^2 \quad (8)$$

ASSOCIATED CONTENT

Supporting information

Electronic properties, transport properties, stability, solubility parameters and additional figures (ionization potential, frontier orbitals, transfer integral, hole mobility, and etc.)

AUTHOR INFORMATION

Corresponding Author

*clemence.corminboeuf@epfl.ch

Author Contributions

The manuscript was written through contributions of all authors. All authors have given approval to the final version of the manuscript. ‡These authors contributed equally.

ACKNOWLEDGMENT

The authors thank the European Research Council (ERC Grant 306528, COMPOREL) for financial support. The authors thank Ganna Gryn'ova, Laurent Vannay and Marko Stojanovic for helpful discussions.

References

(1) Green, M. A.; Ho-Baillie, A.; Snaith, H. J. The Emergence of Perovskite Solar Cells. *Nat. Photonics* **2014**, *8*, 506–514.

(2) Williams, S. T.; Rajagopal, A.; Chueh, C. C.; Jen, A. K. Y. Current Challenges and Prospective Research for Upscaling Hybrid Perovskite Photovoltaics. *J. Phys. Chem. Lett.* **2016**, *7*, 811–819.

(3) Grätzel, M. The Light and Shade of Perovskite Solar Cells. *Nat. Mater.* **2014**, *13*, 838–842.

(4) Huang, L.; Sun, X.; Li, C.; Xu, R.; Xu, J.; Du, Y.; Wu, Y.; Ni, J.; Cai, H.; Li, J.; et al. Electron Transport Layer-Free Planar Perovskite Solar Cells: Further Performance Enhancement Perspective from Device Simulation. *Sol. Energy Mater. Sol. Cells* **2016**, *157*, 1038–1047.

(5) Zhou, H.; Shi, Y.; Dong, Q.; Zhang, H.; Xing, Y.; Wang, K.; Du, Y.; Ma, T. Hole-Conductor-Free, Metal-Electrode-Free TiO2/CH3NH3PbI3 Heterojunction Solar Cells Based on a Low-Temperature Carbon Electrode. *J. Phys. Chem. Lett.* **2014**, *5*, 3241–3246.

(6) Stranks, S. D.; Eperon, G. E.; Grancini, G.; Menelaou, C.; Alcocer, M. J. P.; Leijtens, T.; Herz, L. M.; Petrozza, A.; Snaith, H. J. Electron-Hole Diffusion Lengths Exceeding 1 Micrometer in an Organometal Trihalide Perovskite Absorber. *Science (80-.).* **2013**, *342*, 341–344.

(7) Dongxue, L.; Liu, Y. Recent Progress of Dopant-Free Organic Hole-Transporting Materials in Perovskite Solar Cells. *J. Semicond.* **2017**, *38*, 11005.

(8) Juarez-Perez, E. J.; Wuβler, M.; Fabregat-Santiago, F.; Lakus-Wollny, K.; Mankel, E.; Mayer, T.; Jaegermann, W.; Mora-Sero, I. Role of the Selective Contacts in the Performance of Lead Halide Perovskite Solar Cells. *J. Phys. Chem. Lett.* **2014**, *5*, 680–685.

(9) Bakr, Z. H.; Wali, Q.; Fakharuddin, A.; Schmidt-Mende, L.; Brown, T. M.; Jose, R. Advances in Hole Transport Materials Engineering for Stable and Efficient Perovskite Solar Cells. *Nano Energy* **2017**, *34*, 271–305.

(10) Chi, W.; Sun, P.-P.; Li, Z.-S. A Strategy to Improve the Efficiency of Hole Transporting Materials: Introduction of a Highly Symmetrical Core. *Nanoscale* **2016**, *8*, 17752–17756.

(11) Saliba, M.; Orlandi, S.; Matsui, T.; Aghazada, S.; Cavazzini, M.; Correa-Baena, J.-P.; Gao, P.; Scopelliti, R.; Mosconi, E.; Dahmen, K.-H.; et al. A Molecularly Engineered Hole-Transporting Material for Efficient Perovskite Solar Cells. *Nat. Energy* **2016**, *1*, 15017.

(12) Kim, H.-S.; Lee, C.-R.; Im, J.-H.; Lee, K.-B.; Moehl, T.; Marchioro, A.; Moon, S.-J.; Humphry-Baker, R.; Yum, J.-H.; Moser, J. E.; et al. Lead Iodide Perovskite Sensitized All-Solid-State Submicron Thin Film Mesoscopic Solar Cell with Efficiency Exceeding 9%. *Sci. Rep.* **2012**, *2*, 591.

(13) Ganesan, P.; Fu, K.; Gao, P.; Raabe, I.; Schenk, K.; Scopelliti, R.; Luo, J.; Wong, L. H.; Grätzel, M.; Nazeeruddin, M. K. A Simple Spiro-Type Hole Transporting Material for Efficient Perovskite Solar Cells. *Energy Environ. Sci.* **2015**, *8*, 1986–1991.

(14) Zhang, F.; Liu, X.; Yi, C.; Bi, D.; Luo, J.; Wang, S.; Li, X.; Xiao, Y.; Zakeeruddin, S. M.; Grätzel, M. Dopant-Free Donor (D)-π-D-π-D Conjugated Hole-Transport Materials for Efficient and Stable Perovskite Solar Cells. *ChemSusChem* **2016**, *9*, 2578–2585.

(15) Xue, Y.; Wu, Y.; Li, Y. Readily Synthesized Dopant-Free Hole Transport Materials with Phenol Core for Stabilized Mixed Perovskite Solar Cells. *J. Power Sources* **2017**, *344*, 160–169.

(16) Swetha, T.; Singh, S. P. Perovskite Solar Cells Based on Small Molecules Hole Transporting Materials. *J. Mater. Chem. A* **2015**, *0*, 1–16.

(17) Poplavskyy, D.; Nelson, J. Nondispersive Hole Transport in Amorphous Films of Methoxy-Spirofluorene-Arylamine Organic Compound. *J. Appl. Phys.* **2003**, *93*, 341–346.

(18) Xi, H.; Tang, S.; Ma, X.; Chang, J.; Chen, D.; Lin, Z.; Zhong, P.; Wang, H.; Zhang, C. Performance Enhancement of Planar Heterojunction Perovskite Solar Cells through Tuning the Doping Properties of Hole-Transporting Materials. *ACS Omega* **2017**, *2*, 326–336.

(19) Jeon, N. J.; Lee, J.; Noh, J. H.; Nazeeruddin, K.; Grätzel, M.; Seok, S. Il; Nazeeruddin, M. K.; Grätzel, M.; Seok, S. Il. Efficient Inorganic–Organic Hybrid Perovskite Solar Cells Based on Pyrene Arylamine Derivatives as Hole-Transporting Materials. *J. Am. Chem. Soc.* **2013**, *135*, 19087–19090.

(20) Liu, J.; Wu, Y.; Qin, C.; Yang, X.; Yasuda, T.; Islam, A.; Zhang, K.; Peng, W.; Chen, W.; Han, L. A Dopant-Free Hole-Transporting Material for Efficient and Stable Perovskite Solar Cells. *Energy Environ. Sci.* **2014**, *7*, 2963–2967.

(21) Kazim, S.; Ramos, F. J.; Gao, P.; Nazeeruddin, M. K.; Grä Tzel, M.; Ahmad, S. A Dopant Free Linear Acene Derivative as a Hole Transport Material for Perovskite Pigmented Solar Cells. *Energy Environ. Sci. Energy Environ. Sci* **2015**, *8*, 1816–1823.

(22) Kim, G.-W.; Kang, G.; Kim, J.; Lee, G. Y.; Kim, H. Il; Pyeon, L.; Lee, J.; Park, T. Dopant-Free Polymeric Hole Transport Material for Highly Efficient and Stable Perovskite Solar Cells. *Energy Environ. Sci.* **2016**, *9*, 2326–2333.

(23) Liu, Y.; Chen, Q.; Duan, H.-S.; Zhou, H.; Yang, Y.; Chen, H.; Luo, S.; Song, T.-B.; Dou, L.; Hong, Z.; et al. A Dopant-Free Organic Hole Transport Material for Efficient Planar Heterojunction Perovskite Solar Cells. *J. Mater. Chem. A* **2015**, *3*, 11940–11947.

(24) Zhang, F.; Yi, C.; Wei, P.; Bi, X.; Luo, J.; Jacopin, G.; Wang, S.; Li, X.; Xiao, Y.; Zakeeruddin, S. M.; et al. A Novel Dopant-Free Triphenylamine Based Molecular "Butterfly" Hole-Transport Material for Highly Efficient and Stable Perovskite Solar Cells. *Adv. Energy Mater.* **2016**, *6*, 1600401.

(25) Huang, C.; Fu, W.; Li, C. Z.; Zhang, Z.; Qiu, W.; Shi, M.; Heremans, P.; Jen, A. K. Y.; Chen, H. Dopant-Free Hole-Transporting Material with a C3h Symmetrical Truxene Core for Highly Efficient Perovskite Solar Cells. *J. Am. Chem. Soc.* **2016**, *138*, 2528–2531.

(26) Liu, J.; Wu, Y.; Qin, C.; Yang, X.; Yasuda, T.; Islam, A.; Zhang, K.; Peng, W.; Chen, W.; Han, L. A Dopant-Free Hole-Transporting Material for Efficient and Stable Perovskite Solar Cells. *Energy Environ. Sci.* **2014**, *7*, 2963–2967.

(27) Rakstys, K.; Abate, A.; Dar, M. I.; Gao, P.; Jankauskas, V.; Jacopin, G.; Kamarauskas, E.; Kazim, S.; Ahmad, S.; Grätzel, M.; et al. Triazatruxene-Based Hole Transporting Materials for Highly Efficient Perovskite Solar Cells. *J. Am. Chem. Soc.* **2015**, *137*, 16172–16178.

(28) Wang, J.; Chen, Y.; Liang, M.; Ge, G.; Zhou, R.; Sun, Z.; Xue, S. A New Thermal-Stable Truxene-Based Hole-Transporting Material for Perovskite Solar Cells. *Dye. Pigment.* **2016**, *125*, 399–406.

(29) Goubard, F.; Dumur, F. Truxene: A Promising Scaffold for Future Materials. *RSC Adv.* **2015**, *5*, 3521–3551.

(30) Li, X.-C.; Zhang, Y.; Wang, C.-Y.; Wan, Y.; Lai, W.-Y.; Pang, H.; Huang, W. Redox-Active Triazatruxene-Based Conjugated Microporous Polymers for High-Performance Supercapacitors. *Chem. Sci.* **2017**, *8*, 2959–2965.

(31) Ramos, F. J.; Rakstys, K.; Kazim, S.; Gratzel, M.; Nazeeruddin, M. K.; Ahmad, S. Rational Design of Triazatruxene-Based Hole Conductors for Perovskite Solar Cells. *RSC Adv.* **2015**, *5*, 53426–53432.

(32) Petrikyte, I.; Zimmermann, I.; Rakstys, K.; Daskeviciene, M.; Malinauskas, T.; Jankauskas, V.; Getautis, V.; Nazeeruddin, M. K. Efficiency Enhancement of Perovskite Solar Cells via Incorporation of Phenylethenyl Side Arms into Indolocarbazole-Based Hole Transporting Materials. *Nanoscale* **2016**, *8*, 8530–8535.

(33) Rakstys, K.; Paek, S.; Gao, P.; Gratia, P.; Marszalek, T.; Grancini, G.; Cho, K. T.; Genevicius, K.; Jankauskas, V.; Pisula, W.; et al. Molecular Engineering of Face-on Oriented Dopant-Free Hole Transporting Material for Perovskite Solar Cells with 19% PCE. *J. Mater. Chem. A* **2017**, *5*, 7811–7815.

(34) Su, P.-Y.; Huang, L.-B.; Liu, J.-M.; Chen, Y.-F.; Xiao, L.-M.; Kuang, D.-B.; Mayor, M.; Su, C.-Y. A Multifunctional Poly-N-Vinylcarbazole Interlayer in Perovskite Solar Cells for

High Stability and Efficiency: A Test with New Triazatruxene-Based Hole Transporting Materials. *J. Mater. Chem. A* **2017**, *5*, 1913–1918.

(35) Alberga, D.; Mangiatordi, G. F.; Labat, F.; Ciofini, I.; Nicolotti, O.; Lattanzi, G.; Adamo, C. Theoretical Investigation of Hole Transporter Materials for Energy Devices. *J. Phys. Chem. C* **2015**, *119*, 23890–23898.

(36) Petrus, M. L.; Bein, T.; Dingemans, T. J.; Docampo, P. A Low Cost Azomethine-Based Hole Transporting Material for Perovskite Photovoltaics. *J. Mater. Chem. A* **2015**, *3*, 12159–12162.

(37) Ryu, S.; Noh, J. H.; Jeon, N. J.; Kim, Y. C.; Yang, W. S.; Seo, J.; Seok, S. Il. Voltage Output of Efficient Perovskite Solar Cells with High Open-Circuit Voltage and Fill Factor. *Energy Environ. Sci.* **2014**, *7*, 2614–2618.

(38) Antoine, K. Fermi Level, Work Function and Vacuum Level. *Mater. Horizons* **2015**, *1*, 96.

(39) Bredas, J.-L. Mind the Gap! *Mater. Horiz.* **2014**, *1*, 17–19.

(40) Polander, L. E.; Pahner, P.; Schwarze, M.; Saalfrank, M.; Koerner, C.; Leo, K. Hole-Transport Material Variation in Fully Vacuum Deposited Perovskite Solar Cells. *APL Mater.* **2014**, *2*, 81503.

(41) Savva, A.; Burgués-Ceballos, I.; Choulis, S. A. Improved Performance and Reliability of P-I-N Perovskite Solar Cells via Doped Metal Oxides. *Adv. Energy Mater.* **2016**, *6*, 1600285.

(42) Jiang, Y.; Almansouri, I.; Huang, S.; Young, T.; Li, Y.; Peng, Y.; Hou, Q.; Spiccia, L.; Bach, U.; Cheng, Y.-B.; et al. Optical Analysis of Perovskite/Silicon Tandem Solar Cells. *J. Mater. Chem. C* **2016**, *4*, 5679–5689.

(43) Ameen, S.; Rub, M. A.; Kosa, S. A.; Alamry, K. A.; Akhtar, M. S.; Shin, H.-S.; Seo, H.-K.; Asiri, A. M.; Nazeeruddin, M. K. Perovskite Solar Cells: Influence of Hole Transporting Materials on Power Conversion Efficiency. *ChemSusChem* **2016**, *9*, 10–27.

(44) Calió, L.; Kazim, S.; Grätzel, M.; Ahmad, S. Hole-Transport Materials for Perovskite Solar Cells. *Angew. Chemie Int. Ed.* **2016**, *55*, 14522–14545.

(45) Chi, W.-J.; Li, Q.-S.; Li, Z.-S. Effects of Molecular Configuration on Charge Diffusion Kinetics within Hole-Transporting Materials for Perovskites Solar Cells. *J. Phys. Chem. C* **2015**, *119*, 8584–8590.

(46) Leijtens, T.; Giovenzana, T.; Habisreutinger, S. N.; Tinkham, J. S.; Noel, N. K.; Kamino, B. A.; Sadoughi, G.; Sellinger, A.; Snaith, H. J. Hydrophobic Organic Hole Transporters for Improved Moisture Resistance in Metal Halide Perovskite Solar Cells. *ACS Appl. Mater. Interfaces* **2016**, *8*, 5981–5989.

(47) Zheng, L.; Chung, Y.-H.; Ma, Y.; Zhang, L.; Xiao, L.; Chen, Z.; Wang, S.; Qu, B.; Gong, Q. A Hydrophobic Hole Transporting Oligothiophene for Planar Perovskite Solar Cells with Improved Stability. *Chem. Commun.* **2014**, *50*, 11196.

(48) Kwon, Y. S.; Lim, J.; Yun, H.-J.; Kim, Y.-H.; Park, T. A Diketopyrrolopyrrole-Containing Hole Transporting Conjugated Polymer for Use in Efficient Stable Organic–inorganic Hybrid Solar Cells Based on a Perovskite. *Energy Environ. Sci.* **2014**, *7*, 1454.

(49) Zhang, F.; Zhao, X.; Yi, C.; Bi, D.; Bi, X.; Wei, P.; Liu, X.; Wang, S.; Li, X.; Zakeeruddin, S. M.; et al. Dopant-Free Star-Shaped Hole-Transport Materials for Efficient and Stable Perovskite Solar Cells. *Dye. Pigment.* **2017**, *136*, 273–277.

(50) Su, P. Y.; Chen, Y. F.; Liu, J. M.; Xiao, L. M.; Kuang, D. Bin; Mayor, M.; Su, C. Y. Hydrophobic Hole-Transporting Materials Incorporating Multiple Thiophene Cores with Long Alkyl Chains for Efficient Perovskite Solar Cells. *Electrochim. Acta* **2016**, *209*, 529–540.

(51) Bi, C.; Wang, Q.; Shao, Y.; Yuan, Y.; Xiao, Z.; Huang, J. Non-Wetting Surface-Driven High-Aspect-Ratio Crystalline Grain Growth for Efficient Hybrid Perovskite Solar Cells. *Nat. Commun.* **2015**, *6*, 7747.

(52) Malinauskas, T.; Tomkute-Luksiene, D.; Sens, R.; Daskeviciene, M.; Send, R.; Wonneberger, H.; Jankauskas, V.; Bruder, I.; Getautis, V. Enhancing Thermal Stability and Lifetime of Solid-State Dye-Sensitized Solar Cells via Molecular Engineering of the Hole-Transporting Material Spiro-OMeTAD. *ACS Appl. Mater. Interfaces* **2015**, *7*, 11107–11116.

(53) Luo, J.; Zhao, B.; Shao, J.; Lim, K. A.; On Chan, H. S.; Chi, C. Room-Temperature Discotic Liquid Crystals Based on Oligothiophenes—attached and Fused Triazatruxenes. *J. Mater. Chem.* **2009**, *19*, 8327.

(54) Kumar, S. Monomeric Discotic Liquid Crystals. In *Chemistry of Discotic Liquid Crystals: From Monomers to Polymers*; Liquid Crystals Book Series; CRC Press, 2010; pp 49–360.

(55) Hutchison, G. R.; Ratner, M. A.; Marks, T. J. Intermolecular Charge Transfer between Heterocyclic Oligomers. Effects of Heteroatom and Molecular Packing on Hopping Transport in Organic Semiconductors. *J. Am. Chem. Soc.* **2005**, *127*, 16866–16881.

(56) Gryn'ova, G.; Corminboeuf, C. Implications of Charge Penetration for Heteroatom-Containing Organic Semiconductors. *J. Phys. Chem. Lett.* **2016**, *7*, 5198–5204.

(57) Shelton, S. W.; Chen, T. L.; Barclay, D. E.; Ma, B. Solution-Processable Triindoles as Hole Selective Materials in Organic Solar Cells. *ACS Appl. Mater. Interfaces* **2012**, *4*, 2534–2540.

(58) Ma, Z.; Geng, H.; Wang, D.; Shuai, Z. Influence of Alkyl Side-Chain Length on the Carrier Mobility in Organic Semiconductors: Herringbone vs. Pi–pi Stacking. *J. Mater. Chem. C* **2016**, *4*, 4546–4555.

(59) Cherniawski, B. P.; Lopez, S. A.; Burnett, E. K.; Yavuz, I.; Zhang, L.; Parkin, S. R.; Houk, K. N.; Briseno, A. L. The Effect of Hexyl Side Chains on Molecular Conformations, Crystal Packing, and Charge Transport of Oligothiophenes. *J. Mater. Chem. C* **2017**, *5*, 582–588.

(60) Zhang, J.; Hua, Y.; Xu, B.; Yang, L.; Liu, P.; Johansson, M. B.; Vlachopoulos, N.; Kloo, L.; Boschloo, G.; Johansson, E. M. J.; et al. The Role of 3D Molecular Structural Control in New Hole Transport Materials Outperforming Spiro-OMeTAD in Perovskite Solar Cells. *Adv. Energy Mater.* **2016**, *6*, 1–9.

(61) Chi, W.-J.; Li, Q.-S.; Li, Z.-S. Exploring the Electrochemical Properties of Hole Transport Materials with Spiro-Cores for Efficient Perovskite Solar Cells from First-Principles. *Nanoscale* **2016**, *8*, 6146–6154.

(62) Chi, W.-J.; Sun, P.-P.; Li, Z.-S. How to Regulate Energy Levels and Hole Mobility of Spiro-Type Hole Transport Materials in Perovskite Solar Cells. *Phys. Chem. Chem. Phys.* **2016**, *18*.

(63) AM1.5 solar spectral irradiance. AM1.5 solar spectral irradiance http://rredc.nrel.gov/solar/spectra/am1.5/ASTMG173/ASTMG173.html (accessed Mar 1, 2017).

(64) Fantacci, S.; Angelis, F. De; Nazeeruddin, M. K.; Grätzel, M. Electronic and Optical Properties of the Spiro- MeOTAD Hole Conductor in Its Neutral and Oxidized Forms : A DFT / TDDFT Investigation. *J. Phys. Chem. C* **2011**, *115*, 23126–23133.

(65) Barbara, P. F.; Meyer, T. J.; Ratner, M. a. Contemporary Issues in Electron Transfer Research. *J. Phys. Chem.* **1996**, *100*, 13148–13168.

(66) Marcus, R. a. Electron Transfer Reactions in Chemistry: Theory and Experiment. *Angew. Chemie Int. Ed. English* **1993**, *32*, 1111–1121.

(67) Bässler, H. Charge Transport in Disordered Organic Photoconductors a Monte Carlo Simulation Study. *Phys. status solidi* **1993**, *175*, 15–56.

(68) Coehoorn, R.; Pasveer, W. F.; Bobbert, P. A.; Michels, M. A. J. Charge-Carrier Concentration Dependence of the Hopping Mobility in Organic Materials with Gaussian Disorder. *Phys. Rev. B - Condens. Matter Mater. Phys.* **2005**, *72*, 1–20.

(69) Rühle, V.; Lukyanov, A.; May, F.; Schrader, M.; Vehoff, T.; Kirkpatrick, J.; Baumeier, B.; Andrienko, D. Microscopic Simulations of Charge Transport in Disordered Organic Semiconductors. *J. Chem. Theory Comput.* **2011**, *7*, 3335–3345.

(70) Buchholz, J.; Paul, W.; Varnik, F.; Binder, K. Cooling Rate Dependence of the Glass Transition Temperature of Polymer Melts: Molecular Dynamics Study. *J. Chem. Phys.* **2002**, *117*, 7364.

(71) Sonntag, M.; Kreger, K.; Hanft, D.; Strohriegl, P.; Setayesh, S.; de Leeuw, D. Novel Star-Shaped Triphenylamine-Based Molecular Glasses and Their Use in OFETs. *Chem. Mater.* **2005**, *17*, 3031–3039.

(72) Rogers, S.; Mandelkern, L. Glass Transitions of the Poly-(N-Alkyl Methacrylates). *J. Phys. Chem.* **1957**, *61*, 985–991.

(73) Hildebrand, J. H. The Entropy of Solution of Molecules of Different Size. *J. Chem. Phys.* **1947**, *15*, 225.

(74) Hansen, C. M. The Three Dimensional Solubility Parameter and Solvent Diffusion Coefficient. Their Importance in Surface Coating Formulation. *J. Paint Technol.* **1967**, *39*, 104.

(75) Tummala, N. R.; Bruner, C.; Risko, C.; Brédas, J.-L.; Dauskardt, R. H. Molecular-Scale Understanding of Cohesion and Fracture in P3HT:Fullerene Blends. *ACS Appl. Mater. Interfaces* **2015**, *7*, 9957–9964.

(76) Tummala, N. R.; Mehraeen, S.; Fu, Y.-T.; Risko, C.; Brédas, J.-L. Materials-Scale Implications of Solvent and Temperature on [6,6]-Phenyl-C61-Butyric Acid Methyl Ester (PCBM): A Theoretical Perspective. *Adv. Funct. Mater.* **2013**, *23*, 5800–5813.

(77) Yalkowsky, S.; He, Y.; Jain, P. *Handbook of Aqueous Solubility Data, Second Edition*; CRC Press, 2010.

(78) Stephens, P. J.; Devlin, F. J.; Chabalowski, C. F.; Frisch, M. J. Ab Initio Calculation of Vibrational Absorption and Circular Dichroism Spectra Using Density Functional Force Fields. *J. Phys. Chem.* **1994**, *98*, 11623–11627.

(79) Becke, A. D. Density-functional Thermochemistry. III. The Role of Exact Exchange. *J. Chem. Phys.* **1993**, *98*, 5648–5652.

(80) Grimme, S.; Ehrlich, S.; Goerigk, L. Effect of the Damping Function in Dispersion Corrected Density Functional Theory. *J. Comput. Chem.* **2011**, *32*, 1456–1465.

(81) Frisch, M. J.; Trucks, G. W.; Schlegel, H. B.; Scuseria, G. E.; Robb, M. A.; Cheeseman, J. R.; Scalmani, G.; Barone, V.; Mennucci, B.; Petersson, G. A.; et al. Gaussian 09, Revision D.01. *Gaussian Inc.* **2009**, Wallingford CT.

(82) Cossi, M.; Rega, N.; Scalmani, G.; Barone, V. Energies, Structures, and Electronic Properties of Molecules in Solution with the C-PCM Solvation Model. *J. Comput. Chem.* **2003**, *24*, 669–681.

(83) Martínez, L.; Andrade, R.; Birgin, E. G.; Martínez, J. M. PACKMOL: A Package for Building Initial Configurations for Molecular Dynamics Simulations. *J. Comput. Chem.* **2009**, *30*, 2157–2164.

(84) Van Der Spoel, D.; Lindahl, E.; Hess, B.; Groenhof, G.; Mark, A. E.; Berendsen, H. J. C. GROMACS: Fast, Flexible, and Free. *J. Comput. Chem.* **2005**, *26*, 1701–1718.

(85) Berendsen, H. J. C.; van der Spoel, D.; van Drunen, R. GROMACS: A Message-Passing Parallel Molecular Dynamics Implementation. *Comput. Phys. Commun.* **1995**, *91*, 43–56.

(86) Abraham, M. J.; Murtola, T.; Schulz, R.; Páll, S.; Smith, J. C.; Hess, B.; Lindahl, E. GROMACS: High Performance Molecular Simulations through Multi-Level Parallelism from Laptops to Supercomputers. *SoftwareX* **2015**, *1–2*, 19–25.

(87) Vanommeslaeghe, K.; Hatcher, E.; Acharya, C.; Kundu, S.; Zhong, S.; Shim, J.; Darian, E.; Guvench, O.; Lopes, P.; Vorobyov, I.; et al. CHARMM General Force Field: A Force Field for Drug-like Molecules Compatible with the CHARMM All-Atom Additive Biological Force Fields. *J. Comput. Chem.* **2009**, *31*, NA-NA.

(88) Yu, W.; He, X.; Vanommeslaeghe, K.; MacKerell, A. D. Extension of the CHARMM General Force Field to Sulfonyl-Containing Compounds and Its Utility in Biomolecular Simulations. *J. Comput. Chem.* **2012**, *33*, 2451–2468.

(89) Bayly, C. I.; Cieplak, P.; Cornell, W.; Kollman, P. a. A Well-Behaved Electrostatic Potential Based Method Using Charge Restraints for Deriving Atomic Charges: The RESP Model. *J. Phys. Chem.* **1993**, *97*, 10269–10280.

(90) Bussi, G.; Donadio, D.; Parrinello, M. Canonical Sampling through Velocity Rescaling. *J. Chem. Phys.* **2007**, *126*.

(91) Rühle, V.; Junghans, C.; Lukyanov, A.; Kremer, K.; Andrienko, D. Versatile Object-Oriented Toolkit for Coarse-Graining Applications. *J. Chem. Theory Comput.* **2009**, *5*, 3211–3223.

(92) Carey, C.; Chirlian, L. E.; Francl, M. M.; Gange, D. M. Beyond CHELP: Improved Potential Derived Charges for Sugars. *Glycoconj. J.* **1997**, *14*, 501–505.

(93) Kirkpatrick, J. An Approximate Method for Calculating Transfer Integrals Based on the ZINDO Hamiltonian. *Int. J. Quantum Chem.* **2008**, *108*, 51–56.

(94) Liu, H.; Li, Y.; Krause, W. E.; Rojas, O. J.; Pasquinelli, M. A. The Soft-Confined Method for Creating Molecular Models of Amorphous Polymer Surfaces. *J. Phys. Chem. B* **2012**, *116*, 1570–1578.

(95) Berendsen, H. J. C.; Postma, J. P. M.; Gunsteren, W. F. van; Hermans, J. *Intermolecular Forces*; Pullman, B., Ed.; Reidel: Dordrecht, 1981.

(96) Hirvi, J. T.; Pakkanen, T. A. Molecular Dynamics Simulations of Water Droplets on Polymer Surfaces. *J. Chem. Phys.* **2006**, *125*, 144712.

Table of Content